

1 **Evidence of subduction related thermal and compositional**  
2 **heterogeneity below the United States from transition-zone**  
3 **receiver functions**

4 **Ross Maguire<sup>1</sup>, Jeroen Ritsema<sup>1</sup>, Saskia Goes<sup>2</sup>**

5 <sup>1</sup>Department of Earth and Environmental Sciences, University of Michigan, Ann Arbor, MI, 48109-1005, USA

6 <sup>2</sup>Department of Earth Science and Engineering, Imperial College London, London, SW7 2AZ, United Kingdom

Author Manuscript

This is the author manuscript accepted for publication and has undergone full peer review but has not been through the copyediting, typesetting, pagination and proofreading process, which may lead to differences between this version and the [Version of Record](#). Please cite this article as doi: [10.1029/2018GL078378](https://doi.org/10.1029/2018GL078378)

Corresponding author: Ross Maguire, [romaguir@umich.edu](mailto:romaguir@umich.edu)

## Abstract

The subduction of the Farallon Plate has altered the temperature and composition of the mantle transition zone (MTZ) beneath the United States. We investigate MTZ structure by mapping P-to-S conversions at mineralogical phase changes using USArray waveform data and theoretical seismic profiles based on experimental constraints of phase transition properties as a function of temperature and composition. The width of the MTZ varies by about 35 km over the study region, corresponding to a temperature variation of more than 300 K. The MTZ is coldest and thickest beneath the eastern US where high shear velocity anomalies are tomographically resolved. We detect intermittent P-to-S conversions at depths of 520 km and 730 km. The conversions at 730 km depth are coherent beneath the southeastern United States and are consistent with basalt enrichment of about 50%, possibly due to the emplacement of a fragment of an oceanic plateau (i.e., the Hess conjugate).

## 1 Introduction

The subduction of oceanic lithosphere brings thermal and compositional heterogeneity into the mantle transition zone (MTZ). The transitions to denser mineral phases occur at different pressures in the different chemical components of the slab, including sediments, crust and the depleted mantle lithosphere. Over geologic time, mechanical mixing may produce a compositional gradient across the MTZ since basaltic components accumulate preferentially above the 660-km phase transition and melt-depleted, harzburgitic components concentrate below it [e.g., *Mambole and Fleitout, 2002; Xie and Tackley, 2004; Nakagawa et al., 2010*]. Large fragments of recently subducted slabs may still be intact and distributed within the MTZ.

North America is an ideal region for studying the structure of the MTZ and its modification by plate subduction in the Cenozoic and Mesozoic. Tomographic images of the mantle beneath North America [e.g., *Grand, 1994; van der Lee and Nolet, 1997; Sigloch et al., 2008; Sigloch, 2012; Porritt et al., 2014; Schmandt and Lin, 2014a; Burdick and Lekić, 2017*] reveal high-velocity anomalies within or just below the MTZ beneath the central and eastern United States which may be relics of the Farallon oceanic plate. A phase of low-angle (i.e., flat-slab) subduction may explain the distribution of these slab remnants far from the ancient trench axis and the eastward propagation of deformation and arc-like magmatism during the Laramide orogeny [e.g., *Coney and Reynolds, 1977; Humphreys et al., 2003*]. *Livaccari et al. [1981]* suggested that the subduction of an oceanic

39 plateau may provide the necessary buoyancy since the thickened oceanic crust and de-  
40 pleted harzburgite residue are less dense than the surrounding mantle. *Liu et al.* [2010]  
41 suggested that buoyancy forces from the conjugate halves of the Shatsky Rise and Hess  
42 Rise play a critical role in flat-slab subduction of the Farallon plate. They predicted that  
43 the subducted oceanic plateaus are presently located at the top of the lower mantle be-  
44 neath the southeastern US (the Hess conjugate) and to the east of the Great Lakes region  
45 (the Shatsky conjugate). *Wang et al.* [2017] suggested that the eclogitized Hess conjugate  
46 caused Laramide age subsidence in the Gulf of Mexico region.

47 The deployment of the USArray since 2004 has produced new seismic data for imag-  
48 ing the mantle with high spatial resolution. The USArray includes 120 Reference Network  
49 stations and about 400 Transportable Array stations with about 70-km station spacing. The  
50 TA stations were redeployed at sites in the western US and the eastern US between 2004  
51 and 2013. Building on previous analyses we develop receiver function images from US-  
52 Array waveform data to map seismic discontinuities in the MTZ. Using mineral-physics  
53 relationships between temperature, composition, and seismic velocity, we associate the  
54 discontinuities with mineral phase transitions and estimate variations in temperature and  
55 composition from their relative depths and strengths. In particular, we investigate whether  
56 fragments of relatively cold slabs and relatively dense oceanic plateaus at the base of the  
57 MTZ, are evident in receiver functions to corroborate previous tomographic and geody-  
58 namic observations.

## 59 **2 Receiver functions**

### 60 **2.1 Method**

61 As is well documented [e.g., *Shearer, 2000; Deuss et al., 2013*], phase transitions  
62 in the olivine system produce sharp gradients in seismic velocity observed near depths of  
63 410 km, 520 km, and 660 km. Additional seismic discontinuities have been observed near  
64 the base of the transition zone between 660 km and about 750 km depth [e.g., *Simmons*  
65 *and Gurrola, 2000; Deuss et al., 2006; Wang and Niu, 2011*], which are commonly inter-  
66 preted as phase transitions in the garnet system, although a post-stishovite phase transition  
67 may be important in subduction settings [*Tauzin et al., 2018*]. Since garnet is a primary  
68 constituent in basaltic material at transition zone pressures, the detection of seismic sig-

69 nals produced just below 660-km depth may provide a useful estimate of the basalt con-  
70 tent at the base of the MTZ.

71 In this study, we use the *Pds* receiver function method [e.g., Vinnik, 1977; Burdick  
72 and Langston, 1977; Kind et al., 2012] to image seismic velocity gradients in the MTZ.  
73 The *Pds* phase is a P-to-S wave conversion at depth  $d$ . Its amplitude and arrival time  
74 depends on the impedance contrast and depth of the seismic discontinuities or velocity  
75 gradients associated with mineral phase transitions. We compute receiver functions by ro-  
76 tating the original seismograms into the RTZ coordinate system, filtering the waveforms  
77 with a bandpass filter between periods of 5–50 s, cutting waveform sections that begin  
78 10 s before and end 120 s after the predicted P wave arrivals, and deconvolving the verti-  
79 cal from the radial component waveforms using the time-domain matrix inversion method  
80 [e.g., Gurrola et al., 1995]. The deconvolution is stabilized by using a damping parameter  
81  $\lambda$  (we use  $\lambda = 5$ ) to suppress noise without excessive low-pass filtering.

82 We analyze USArray recordings of all earthquakes which occurred between 2008–  
83 2014 and with moment magnitudes between 6 and 7 (Supplementary Figure 1). We in-  
84 clude event-station pairs for epicentral distances between 30° and 90°. We cull receiver  
85 functions both visually and using the signal-to-noise criterion that the RMS amplitude of a  
86 5-s window centered on the *P* onset must be at least 3 times larger than the RMS ampli-  
87 tude of a 20-s window [Schmandt et al., 2012]. After quality control, roughly half of the  
88 dataset has been rejected, retaining 46,026 high-quality receiver functions.

89 We migrate the receiver functions to depth using the common conversion point  
90 (CCP) technique [e.g., Dueker and Sheehan, 1997; Eagar et al., 2010; Schmandt et al.,  
91 2012; Gao and Liu, 2014]. Voxels in the imaging domain are about  $50 \times 50$  km<sup>2</sup> wide and  
92 2 km thick. At a given depth, receiver function signals contribute to all points in the CCP  
93 volume which are within one Fresnel zone radius of the pierce point. The Fresnel zone  
94 radius is calculated for a 5 s period *S* wave. We estimate and subtract the contributions  
95 of 3D velocity anomalies to the *Pds* and *P* traveltimes by ray tracing through the tomo-  
96 graphic model US-SL-2014 [Schmandt and Lin, 2014a] using the TauP method [Crotwell  
97 et al., 1999]. The distribution of epicentral distances has a slight bias toward larger dis-  
98 tances and the majority of the events were in South America and the western Pacific (see  
99 Supplementary Figure 1). In Supplementary Figure 2, we demonstrate that the imaging

artifacts due to the incomplete illumination geometry do not affect the main conclusions drawn from the analysis.

## 2.2 CCP cross sections

Figure 1 shows vertical cross sections through the CCP image along parallels at latitudes 44°N (profile X), 38°N (profile Y) and 32°N (profile Z). The migrated receiver functions are superposed on the shear velocity structure of US-SL-2014 [Schmandt and Lin, 2014a]. P-to-S conversions from the 410-km and 660-km discontinuities (i.e.,  $P410s$  and  $P660s$ ) are the largest phases and coherent throughout the CCP image. Their amplitudes vary, but on average they are both about 4% of the direct P arrival. Along each cross section, the depths of the 410 and 660 varies by as much as  $\pm 20$  km. Regions with the strongest deflections of the 410 and 660 correspond to strong velocity anomalies in US-SL-2014. In general, regions with a positive velocity anomaly in the transition zone correspond to an anomalously thick MTZ, while the opposite is true for regions with a negative velocity anomaly.

Signals of conversions from near the 520 (i.e.,  $P520s$ ) are detected intermittently in each of the three cross sections (circled in green). In cross section X, a strong 520 between  $-100^\circ$  and  $-110^\circ$  has an amplitude as large as 25% of  $P410s$ , and corresponds to a high velocity anomaly in US-SL2014. Weaker signals from 520 are present in cross section Y in low velocity regions. In cross section Z, the 520 is apparent in several locations but shows no clear association with velocity anomalies. There is an apparent doubling of the 520 near the western end of cross section Z, but the seismic data coverage is poor here and imaging artifacts may be substantial (see Supplemental Figure 2).

Cross section Z shows a strong signal from 730 is present between  $-85^\circ$  and  $-95^\circ$  (circled in pink). Here, the maximum amplitude of  $P730s$  is about 30% of the amplitude of  $P660s$ . This signal coincides with a fast seismic velocity anomaly and a strong 520. Signals from 730 are also present in cross section Y in a region of anomalously high seismic velocity, but with no associated detection of the 520.

The CCP images show complicated signals between 250 km and 400 km depth, with single or double peaked arrivals coherent across broad regions. We do not interpret these signals since synthetic tests indicate the presence of artificial arrivals in this depth range (see Supplemental Information). Negative velocity gradients above the 410 have been

131 previously reported beneath the western United States [e.g., *Schmandt et al.*, 2011; *Hier-*  
132 *Majumder and Tauzin*, 2017] which may be related to upper mantle melting. Sporadic and  
133 weak conversions are present between about 850-km and 1000-km depth. Seismic layer-  
134 ing in the lower mantle have been observed previously [e.g., *Jenkins et al.*, 2017; *Waszek*  
135 *et al.*, 2018], but there are no known mineral phase transitions that could account for these  
136 observations.

### 137 **2.3 Phasing diagrams**

138 We verify that the observed *Pds* conversions from 520-km and 730-km depth have  
139 the expected slownesses by a phasing analysis [e.g., *Fee and Dueker*, 2004] of receiver  
140 functions from regions with the strongest signals. Figure 2 compares the stack of all 46,026  
141 receiver functions (Figure 2A) to stacks of receiver functions that sample the northern  
142 Rockies (Figure 2B) and the southeastern US (Figure 2C). We estimate amplitude uncer-  
143 tainties by bootstrap resampling the receiver function stacks [*Efron and Tibshirani*, 1986].

144 The move-out corrected stack for the full data set (bottom left of Figure 2A) repre-  
145 sents the average transition zone structure beneath the USArray. The *P410s* and *P660s*  
146 conversions at the 410 and 660 are the main signals and have the predicted P-to-S move-  
147 out. The *P520s* and *P730s* conversions are invisible, confirming that the 520 and 730  
148 are not coherent boundaries beneath the USArray. The 520 is detected in the stacks of  
149 both subsets but the 730 is visible only in the stack from the southeastern United States  
150 (Figure 2C). Both the 520 and 730 signals are above noise level according to bootstrap  
151 re-sampling analysis. The phasing analysis diagrams (right panels of Figure 2B and C)  
152 confirm that the signals at 55 s after P (i.e., 9.8 s after *P410s*) and 73 s after P (i.e., 5.5 s  
153 after *P410s*) have slownesses and traveltimes consistent with *P520s* and *P730s*. It is un-  
154 likely that these signals are crustal shear-wave reverberations following *P410s* and *P660s*  
155 since reverberations arrive with the same time delay after *P410s* and *P660s* (see Supple-  
156 mental Figure 3).

## 157 **3 Interpretation**

### 158 **3.1 Modeling temperature and composition dependent velocity**

159 We interpret our receiver function images of the transition zone using mineral physics  
160 modeling of the relationship between temperature, composition, and seismic velocity in

161 the mantle. We compute the effects of temperature and composition on mineral phase  
 162 equilibria and seismic velocities in the MTZ using the thermodynamic code *Perple\_X*  
 163 [*Connolly, 2005*] and the elastic parameter database of *Stixrude and Lithgow-Bertelloni*  
 164 [2011]. To account for the pressure and temperature dependent effects of anelasticity on  
 165 seismic velocity, we correct the anharmonic velocity using the attenuation model Q7g  
 166 [e.g., *Maguire et al., 2016*]. We consider the mantle to be a mechanical mixture of basalt  
 167 (i.e., recycled oceanic crust) and harzburgite (i.e., the melt depleted fraction of oceanic  
 168 lithosphere), which is a valid approximation if the re-equilibration rate of basalt and harzburgite  
 169 is slow compared to the convective time scale [*Xu et al., 2008*]. We refer to the end  
 170 member compositions basalt and harzburgite for simplicity but the actual mineral assem-  
 171 blages depend on thermodynamic conditions. The relative fractions of basalt and harzburgite  
 172 are defined as  $f$  and  $1-f$ . We use the mid-ocean ridge basalt composition from *Work-*  
 173 *man and Hart* [2005] and harzburgite composition from *Baker and Beckett* [1999].

174 Figure 3A shows how the shear wave velocity  $V_S$  depends on the basalt fraction  $f$   
 175 in the mantle. Profiles of the P-wave velocity have a similar character. Each profile of  $V_S$   
 176 is computed along an adiabat with a potential temperature of 1300 K. There are seismic  
 177 discontinuities or sharp gradients near 300 km, 410 km, 520 km, 660 km, and 730 km  
 178 depth. For a pyrolitic (i.e.,  $f \approx 0.2$ ) or harzburgite-enriched mantle ( $f < 0.2$ ), the 410,  
 179 520, and 660 in the olivine system are dominant. Both the 410 and 660 are narrower than  
 180 10 km and they are the largest discontinuities with shear velocity jumps of 7.5 % and 7.2  
 181 % respectively. The 300 and 520 are weaker and the 520 is spread over a broad depth  
 182 interval.

183 As  $f$  increases, the 410, 520 and 660 phase changes in the olivine system weaken  
 184 while the coesite to stishovite transformation near 300 km depth and the majorite garnet  
 185 to bridgmanite transformation near 730 km depth become stronger. Low wave speeds  
 186 throughout the transition zone also characterize a mantle enriched in basalt. The increase  
 187 of  $V_S$  at the 730 is 1.8% for  $f = 0.2$  and 11.1% for  $f = 1$ . The 730 is the only phase tran-  
 188 sition that occurs near the base of the transition zone in a purely basaltic mantle (when  
 189  $f = 1$ ). Since the strength of the 660 and 730 depends strongly on  $f$ , we use the relative  
 190 amplitudes of  $P660s$  and  $P730s$  to estimate the basalt fraction  $f$ . Figure 3B shows am-  
 191 plitude ratios from synthetic receiver functions computed for shear velocity profiles with  
 192 variable  $f$  (see also Supplemental Figure 4).

193 Figure 3C shows how phase changes and  $V_S$  in the upper mantle depend on temper-  
194 ature. Here, we assume a homogeneous mantle composition with  $f = 0.2$  (i.e., a roughly  
195 pyrolitic mantle). We vary the potential temperature of the adiabat between 1000 K and  
196 2000 K, which is within about -600 K to +400 K of the average potential temperature of  
197 mid-ocean-ridge basalt (MORB) suggested by *Herzberg et al.* [2007]. Since the Clapey-  
198 ron slope of the 410 and the 660 are +2.7 MPa/K and -1.3 MPa/K, respectively, the phase  
199 boundary topography of the 660 is much more subdued than the 410 for the same thermal  
200 anomaly and the transition zone thickness varies from 200 km to 325 km for our range of  
201 potential temperatures (Figure 3D).

202 In our modeling, the 730 is a strongly temperature-dependent exothermic transition  
203 with a Clapeyron slope of +5.6 MPa/K. Its depth varies between about 700 km (for the  
204 1000 K adiabat) to greater than 850 km (for the 2000 K adiabat). In principle, the ob-  
205 served depth of the post-garnet transition could constrain temperature at the top of the  
206 lower mantle. However, the experimentally determined Clapeyron slope is highly uncer-  
207 tain, with reported values ranging from +0.8 MPa/K [*Hirose et al.*, 1999] to +6.4 MPa/K  
208 [*Oguri et al.*, 2000]. Additionally,  $P730s$  is generally too weak in our data for it to be use-  
209 ful to map the temperature structure throughout the study region.

### 210 3.2 Transition zone properties

211 Our estimates of the MTZ thickness and temperature inferred from our mineral  
212 physics models are shown in Figure 4A. The thickness of the transition zone is on av-  
213 erage 249 km with peak-to-peak variations of about 35 km. This is in good agreement  
214 with the study by *Gao and Liu* [2014]. The variation in thickness is similar to the velocity  
215 variations at 400 km depth imaged in US-SL-2014 (Figure 4D) and implies that the tem-  
216 perature in the MTZ beneath the United States varies by more than 300 K. Estimates of  
217 transition zone thickness and temperature change slightly depending on the seismic veloc-  
218 ity model used to migrate receiver functions, but the general interpretations are robust (see  
219 Supplemental Figure 5).

220 The transition zone is thinnest and therefore warmest beneath the western United  
221 States, except for the Columbia Plateau region to the east of the Cascades. This likely  
222 reflects the cooling of the mantle by the Juan de Fuca slab which has penetrated into  
223 the MTZ although US-SL-2014 does not provide clear tomographic evidence for a high-

224 velocity anomaly in the MTZ beneath this region. Yellowstone stands out as a small-scale  
225 region with an anomalously thin (230–240 km) transition zone, corresponding to a poten-  
226 tial temperature of 1650–1750 K. It implies a deep origin of the Yellowstone hotspot, in  
227 agreement with *Schmandt et al.* [2012] and *Tauzin et al.* [2013] but not with *Gao and Liu*  
228 [2014], who do not find evidence for a thin transition zone beneath Yellowstone. The tran-  
229 sition zone is relatively thick (260–270 km) over broad regions beneath the central and  
230 southeastern United States with maxima that coincide with high-velocity anomalies in US-  
231 SL-2014. We infer the potential temperature in these regions to be between 1400–1500  
232 K.

233 Figure 4B shows the regions where 520 discontinuity appears to be the strongest.  
234 The amplitude of  $P520s$  is difficult to measure due to interference with the relatively  
235 strong side lobes of  $P410s$  and  $P660s$ , which are artifacts of waveform deconvolution.  
236 Therefore we simply show in Figure 4B the regions where  $P520s$  is at least 20% of  $P410s$ ,  
237 which we consider to be robust detections. The 520 is strong in the MTZ beneath the  
238 Columbia Plateau and northern Basin and Range, where we also resolve the transition  
239 zone to be relatively thick and therefore cold. Further, we detect 520 coherently over a  
240 broad area beneath the northern Great Plains and Rocky Mountain region where wave  
241 speeds are relatively high according to US-SL-2104. However, we do not find evidence  
242 for a cool and thick transition zone in this region, which would be expected if slabs of  
243 subducted material are present. The 520 is also apparent in the southeastern United States  
244 near the Gulf of Mexico. Here, the thick transition zone and the high wave speeds provide  
245 complementary evidence for a cold downwelling.

246 Mineral physics models (Figure 3A) indicate that the impedance contrast at 520 in-  
247 creases with decreasing  $f$ . Therefore, Figure 4B may indicate regions of harzburgite en-  
248 richment. The absence of a pervasive detection of a 520 across the study area could indi-  
249 cate the MTZ is enriched in basalt on average. It is also possible that the intermittent de-  
250 tection of the 520 may signify a local sharpening of the seismic discontinuity, rather than  
251 an increased impedance contrast, which would increase the seismic visibility. Recently,  
252 *Mrosko et al.* [2015] found that the presence of water in transition zone under oxidizing  
253 environment reduces the stability field over which ringwoodite and wadsleyite coexist, and  
254 thus reducing the width of the 520 discontinuity. These conditions are expected in regions  
255 of subduction, and thus may explain the association we observe between detections of the  
256 520 and inferred downwellings, particularly in the southeastern United States. A hydrated

257 transition zone beneath the Gulf of Mexico region has also been suggested by *Courtier*  
258 *and Revenaugh* [2013] who observe a strong 520 using multiple reverberations of *ScS*.

259 Figure 4C shows the variable basalt fraction  $f$  at the base of the MTZ inferred from  
260 amplitude ratios of *P730s* and *P660s*. We assume that  $f = 0$  in regions where *P730s*  
261 is undetected, which may be inaccurate if *P730s* is masked by side-lobes of adjacent ar-  
262 rivals, or if signals stack incoherently due to unmodeled 3D velocity structure. Addition-  
263 ally, regions with negative arrivals below 660, for example due to dehydration melting  
264 [e.g., *Schmandt et al.*, 2014b], would map as regions with  $f = 0$ . Nonetheless, Figure 4C  
265 reveals an intriguing pattern of the basalt content at the base of the transition zone.

266 The inferred basalt enrichment, with values  $f > 0.3$ , is highest in the southeastern  
267 US near the Gulf of Mexico. This coincides with a region of thick transition zone, and a  
268 detection of the 520. Additionally, US-SL-2014 maps a high velocity anomaly at the top  
269 of the lower mantle in this region (Figure 4E). A similarly enriched mantle is found along  
270 the Atlantic coast to the east of the Appalachians with no concurrent detection of the 520.  
271 Small regions of enriched mantle are also found to the east of the Great Lakes region and  
272 near Lake Superior. The western US is largely depleted with the exception of the Col-  
273 orado Plateau region, with  $f \approx 0.2$ , and an east-west trending region north of Rockies with  
274  $f \approx 0.3$ . The Northern Rockies region is also associated with a strong 520.

#### 275 **4 Discussion**

276 In a pyrolitic mantle, the 520 and 730 should produce observable *P520s* and *P730s*  
277 wave conversions (see Supplementary Figure 4), yet these signals are recorded intermit-  
278 tently. The low amplitudes of *P520s* and *P730s* may indicate a strongly compositionally  
279 layered mantle with basalt enrichment and depletion above and below the 660, respectively  
280 [e.g., *Nakagawa et al.*, 2010]. The 520 and 730 are weak or even absent in such a man-  
281 tle. Our stack of the full set of receiver functions from all stations of the USArray is con-  
282 sistent with the geodynamic predictions of a compositional gradient in the MTZ beneath  
283 North America.

284 The local detections of *P520s* and *P730s* may indicate regions of the MTZ where  
285 a compositional gradient has been perturbed by vertical flow, either by sinking slabs or  
286 the ascent of plumes. In general, there is no clear correlation between the strength of the

287 520 and 730 discontinuities and the inferred MTZ temperature, although some trends are  
288 apparent.

- 289 1. The detection of the 520 typically coincides with high-velocity anomalies in US-  
290 SL-2014 within the MTZ, with a thick transition zone, or both.
- 291 2. The MTZ is coolest and the basalt enrichment is highest beneath the eastern US.
- 292 3. Basalt enrichment in the Gulf of Mexico region correlates with a high-velocity  
293 anomaly, a detection of the 520, and a thick transition zone.

294 These results are consistent with a mantle that has been perturbed by recent subduc-  
295 tion and with the widespread distribution of fragments of cold slabs in the MTZ beneath  
296 the eastern US. Previous studies have interpreted the high-velocity anomalies in the MTZ  
297 as remnants of the Farallon slab, which subducted eastward from the western margin of  
298 the US during the Mesozoic and Cenozoic [e.g., *Bunge and Grand, 2000*], although other  
299 subduction histories remain possible [e.g., *Sigloch and Mihalynuk, 2013*].

300 Geodynamic simulations by *Liu et al.* [2010] suggest that buoyancy forces from the  
301 conjugate halves of the Shatsky Rise and Hess Rise play a critical role in flat slab subduc-  
302 tion of the Farallon plate. Furthermore, they predicted that the subducted oceanic plateaus  
303 are presently located at the top of the lower mantle beneath the southeastern United States  
304 (the Hess conjugate) and to the east of the Great Lakes (the Shatsky conjugate). *Wang*  
305 *et al.* [2017] suggested that the negative buoyancy from the eclogitized Hess conjugate  
306 explains Laramide age subsidence in the Gulf of Mexico region. The presence of a sub-  
307 ducted oceanic plateau (i.e., the Hess conjugate) may explain the strong signature of basalt  
308 enrichment that we observe beneath the southeastern US.

## 309 5 Conclusions

310 CCP images (Figures 1 and 4) of receiver functions from seven years of USArray  
311 waveform data indicate the variable strength of phase transitions in the transition zone.  
312 This is compatible with a mantle with basalt enrichment in the MTZ above the 660 and  
313 harzburgite enrichment in the mantle below the 660. The images, with a lateral resolution  
314 of about 100 km, indicate that the 410 and 660 transitions are the only coherent bound-  
315 aries. The width between the 410 and 660 varies by about 35 km, consistent with temper-  
316 ature variations of 300 K. The lateral variations of the apparent transition zone thickness

317 correlate with the wave speed variation resolved by tomography. The transition zone is  
318 relatively thick and cool beneath the eastern United States, due to the presence of frag-  
319 ments of the subducted Farallon slab.

320 The receiver functions include a strong P-wave to S-wave conversion from a depth  
321 of about 730 km beneath the Gulf of Mexico region which is consistent with the gar-  
322 net to bridgmanite phase transition within a relatively cold (1400 – 1500 ° K) slab frag-  
323 ment. The location of the reflector at 730-km depth correlates with the location of the  
324 subducted Hess conjugate predicted by geodynamic simulations [*Liu et al.*, 2010]. Our  
325 results demonstrate the potential of using the regional variability of the transition zone  
326 structure below 660-km depth to map compositional heterogeneity at the base of the tran-  
327 sition zone.

### 328 **Acknowledgments**

329 All seismic data used in this study is available online through the IRIS data service (<http://ds.iris.edu/ds/>).  
330 This research has been funded by NSF grant EAR-1565511 to JR, and NERC project  
331 NE/J008028/1 to SG. RM acknowledges support from Turner Research Funds and the  
332 Rackham Graduate School at UM. The authors thank Benoit Tausin and Stephen Gao for  
333 constructive reviews that improved this study.

### 334 **References**

- 335 Baker, M. B., and J. R. Beckett (1999), The origin of abyssal peridotites: A reinterpret-  
336 ation of constraints based on primary bulk compositions, *Earth and Planetary Science*  
337 *Letters*, *171*(1), 49–61, doi:10.1016/S0012-821X(99)00130-2.
- 338 Bunge, H.-P., and S. P. Grand (2000), Mesozoic plate-motion history below the northeast  
339 pacific ocean from seismic images of the subducted farallon slab, *Nature*, *405*(6784),  
340 337.
- 341 Burdick, L. J., and C. a. Langston (1977), Modeling crustal structure through the use of  
342 converted phases in teleseismic body-wave forms, *Bulletin of the Seismological Society of*  
343 *America*, *67*(3), 677–691.
- 344 Burdick, S., and V. Lekić (2017), Velocity variations and uncertainty from transdimen-  
345 sional P-wave tomography of North America, *Geophysical Journal International*, *209*(2),  
346 1337–1351, doi:10.1093/gji/ggx091.

- 347 Coney, P. J., and S. J. Reynolds (1977), Cordilleran Benioff Zones, *Nature*, 270, 403–406,  
348 doi:10.1038/275464a0.
- 349 Connolly, J. a. D. (2005), Computation of phase equilibria by linear programming: A tool  
350 for geodynamic modeling and its application to subduction zone decarbonation, *Earth  
351 and Planetary Science Letters*, 236(1-2), 524–541, doi:10.1016/j.epsl.2005.04.033.
- 352 Courtier, A. M., and J. Revenaugh (2013), A Water-Rich Transition Zone Beneath the  
353 Eastern United States and Gulf of Mexico from Multiple ScS Reverberations, in *Earth's  
354 Deep Water Cycle*, pp. 181–193, doi:10.1029/168GM14.
- 355 Crotwell, H. P., T. J. Owens, and J. Ritsema (1999), The TauP Toolkit : Flexible Seismic  
356 Travel-time and Ray-path Utilities, *Seismological Research Letters*, 70, 154–160.
- 357 Deuss, A., S. A. T. Redfern, K. Chambers, and J. H. Woodhouse (2006), The Nature of  
358 the 660-Kilometer Discontinuity in Earth's Mantle from Global Seismic Observations of  
359 PP Precursors, *Science*, 311(5758), 198–201, doi:10.1126/science.1120020.
- 360 Deuss, A., J. Andrews, and E. Day (2013), Seismic Observations of Mantle Discontinu-  
361 ities and Their Mineralogical and Dynamical Interpretation, in *Physics and Chemistry of  
362 the Deep Earth*, edited by S.-i. Karato, 1st ed., Wiley and Sons Ltd.
- 363 Dueker, K. G., and A. F. Sheehan (1997), Mantle discontinuity structure from midpoint  
364 stacks of converted P to S waves across the Yellowstone hotspot track, *Journal of Geo-  
365 physical Research*, 102(B4), 8313, doi:10.1029/96JB03857.
- 366 Egar, K. C., M. J. Fouch, and D. E. James (2010), Receiver function imaging of upper  
367 mantle complexity beneath the Pacific Northwest, United States, *Earth and Planetary  
368 Science Letters*, 297(1-2), 141–153, doi:10.1016/j.epsl.2010.06.015.
- 369 Efron, B., and R. Tibshirani (1986), Bootstrap methods for standard error, confidence in-  
370 tervals, and other measures of statistical accuracy, *Statistical Science*, 1(1), 54–75, doi:  
371 10.1214/ss/1177013817.
- 372 Ekström, G., M. Nettles, and A. M. Dziewoński (2012), The global CMT project 2004 –  
373 2010 : Centroid-moment tensors, *Physics of the Earth and Planetary Interiors*, 201, 1–9,  
374 doi:10.1016/j.pepi.2012.04.002.
- 375 Fee, D., and K. Dueker (2004), Mantle transition zone topography and structure be-  
376 neath the Yellowstone hotspot, *Geophysical Research Letters*, 31(18), 1–4, doi:  
377 10.1029/2004GL020636.
- 378 Gao, S. S., and K. H. Liu (2014), Mantle transition zone discontinuities beneath the con-  
379 tiguous United States, *Journal of Geophysical Research: Solid Earth*, pp. 1–17, doi:

- 380 10.1002/2014JB011253.1.
- 381 Grand, S. P. (1994), Mantle shear structure beneath the Americas and surrounding  
382 oceans, *Journal of Geophysical Research: Solid Earth*, 99(B6), 11,591–11,621, doi:  
383 10.1029/94JB00042.
- 384 Gurrola, H., G. Baker, and J. Minister (1995), Simultaneous time-domain deconvolution  
385 with application to the computation of receiver functions, *Geophysical Journal Interna-*  
386 *tional*, 120, 537–543.
- 387 Herzberg, C., P. D. Asimow, N. Arndt, Y. Niu, C. M. Lesher, J. G. Fitton, M. J. Cheadle,  
388 and A. D. Saunders (2007), Temperatures in ambient mantle and plumes: Constraints  
389 from basalts, picrites, and komatiites, *Geochemistry, Geophysics, Geosystems*, 8(2), doi:  
390 10.1029/2006GC001390.
- 391 Hier-Majumder, S., and B. Tauzin (2017) Pervasive upper mantle melting be-  
392 neath the western US, *Earth and Planetary Science Letters* 463, 25–35, doi:  
393 10.1016/j.epsl.2016.12.041
- 394 Hirose, K., Y. Fei, Y. Ma, H.K. Mao (1999), The fate of subducted basaltic crust in the  
395 Earth's lower mantle, *Nature*, 397(6714), 53–56, doi:10.1038/16225
- 396 Humphreys, E., E. Hessler, K. Dueker, G. L. Farmer, E. Erslev, and T. Atwater (2003),  
397 How Laramide-Age Hydration of North American Lithosphere by the Farallon Slab  
398 Controlled Subsequent Activity in the Western United States, *International Geology Re-*  
399 *view*, 45(7), 575–595, doi:10.2747/0020-6814.45.7.575.
- 400 Jenkins, J., A. Deuss, and S. Cottaar (2017), Converted phases from sharp 1000 km depth  
401 mid-mantle heterogeneity beneath Western Europe, *Earth and Planetary Science Letters*,  
402 459, 196–207, doi:10.1016/j.epsl.2016.11.031.
- 403 Kind, R., X. Yuan, and P. Kumar (2012), Seismic receiver functions and the  
404 lithosphere-asthenosphere boundary, *Tectonophysics*, 536-537, 25–43, doi:  
405 10.1016/j.tecto.2012.03.005.
- 406 Laske, G., G. Masters, and C. Reif (2001), Crust2. 0: a new global crustal model at 2 × 2  
407 degrees, *Institute of Geophysics and Planetary Physics, The University of California, San*  
408 *Diego, website <http://mahi.ucsd.edu/Gabi/rem.dir/crust/crust2.html>.*
- 409 Lekić, V., and K. M. Fischer (2017), Interpreting spatially stacked Sp receiver functions,  
410 *Geophysical Journal International*, 210(2), 874–886, doi:10.1093/gji/ggx206.
- 411 Liu, L., M. Gurnis, M. Seton, J. Saleeby, R. D. Müller, and J. M. Jackson (2010), The  
412 role of oceanic plateau subduction in the Laramide orogeny, *Nature Geoscience*, 3(5),

- 413 353–357, doi:10.1038/ngeo829.
- 414 Livaccari, R. F., K. Burke, and A. M. C. Sengör (1981), Was the Laramide  
415 orogeny related to subduction of an oceanic plateau?, *Nature*, 289, 276–278, doi:  
416 10.1038/289276a0.
- 417 Maguire, R., J. Ritsema, P. E. van Keken, A. Fichtner, and S. Goes (2016), P- and S-wave  
418 delays caused by thermal plumes, *Geophysical Journal International*, 206(2), 1169–  
419 1178, doi:10.1093/gji/ggw187.
- 420 Mambole, A., and L. Fleitout (2002), Petrological layering induced by an endothermic  
421 phase transition in the Earth’s mantle, *Geophysical Research Letters*, 29(22), 2–5, doi:  
422 10.1029/2002GL014674.
- 423 Montagner, J.-P., and B. L. N. Kennett (1996), How to reconcile body-wave and normal-  
424 mode reference earth models, *Geophysical Journal International*, 125(1), 229–248, doi:  
425 10.1111/j.1365-246X.1996.tb06548.x.
- 426 Mrosko, M., M. Koch-Müller, C. McCammon, D. Rhede, J. R. Smyth, and R. Wirth  
427 (2015), Water, iron, redox environment: effects on the wadsleyite–ringwoodite  
428 phase transition, *Contributions to Mineralogy and Petrology*, 170(1), 1–12, doi:  
429 10.1007/s00410-015-1163-2.
- 430 Nakagawa, T., P. J. Tackley, F. Deschamps, and J. A. D. Connolly (2010), The influence  
431 of MORB and harzburgite composition on thermo-chemical mantle convection in a 3-  
432 D spherical shell with self-consistently calculated mineral physics, *Earth and Planetary  
433 Science Letters*, 296(3-4), 403–412, doi:10.1016/j.epsl.2010.05.026.
- 434 Nissen-meyer, T., M. Van Driel, S. C. Stähler, K. Hosseini, S. Hempel, L. Auer,  
435 A. Colombi, and A. Fournier (2014), AxiSEM: Broadband 3-D seismic wavefields in  
436 axisymmetric media, *Solid Earth*, 5(1), 425–445, doi:10.5194/se-5-425-2014.
- 437 Oguri, K., N. Funamori, T. Uchida, N. Miyajima, T. Yagi, and K. Fujino (2000), Post-  
438 garnet transition in a natural pyrope: a multi-anvil study based on in situ X-ray diffrac-  
439 tion and transmission electron microscopy *Physics of Earth and Planetary Interiors*, 122,  
440 175–186, doi:10.1016/S0031-9201(00)00178-3
- 441 Porritt, R. W., R. M. Allen, and F. F. Pollitz (2014), Seismic imaging east of the Rocky  
442 Mountains with USArray, *Earth and Planetary Science Letters*, 402(C), 16–25, doi:  
443 10.1016/j.epsl.2013.10.034.
- 444 Schmandt, B., and F.-c. Lin (2014a), P and S wave tomography of the mantle be-  
445 neath the United States, *Geophysical Research Letters*, 41, 6342–6349, doi:

446 10.1002/2014GL061231.

447 Schmandt, B., K. G. Dueker, E. D. Humphreys, and S. Hansen (2012), Hot mantle up-  
448 welling across the 660 beneath Yellowstone, *Earth and Planetary Science Letters*, 331-  
449 332, 224–236, doi:10.1016/j.epsl.2012.03.025.

450 Schmandt, B., S. D. Jacobsen, T. W. Becker, Z. Liu, and K. G. Dueker (2014b), Dehydra-  
451 tion melting at the top of the lower mantle, *Science*, 344(6189), 1265–1268.

452 Schmandt, B., K. G. Dueker, S. M. Hansen, J. J. Jasbinsek, and Z. Zhang (2011), A  
453 sporadic low-velocity layer atop the western U.S. mantle transition zone and short-  
454 wavelength variations in transition zone discontinuities, *Geochemistry, Geophysics,*  
455 *Geosystems*, 12, doi:10.1029/2011GC003668

456 Shearer, P. (2000), Upper mantle seismic discontinuities, in *Earth's Deep Interior: Min-*  
457 *eral Physics and Tomography From the Atomic to Global Scale*, pp. 115–131, doi:  
458 10.1016/0031-9201(95)03059-6.

459 Sigloch, K. (2012), Mantle provinces under North America from multifrequency  
460 P wave tomography, *Geochemistry, Geophysics, Geosystems*, 12(2), 1–27, doi:  
461 10.1029/2010GC003421.

462 Sigloch, K., and M. G. Mihalynuk (2013), Intra-oceanic subduction shaped the assembly  
463 of Cordilleran North America, *Nature*, 496(7443), 50–56, doi:10.1038/nature12019.

464 Sigloch, K., N. McQuarrie, and G. Nolet (2008), Two-stage subduction history under  
465 North America inferred from multiple-frequency tomography, *Nature Geoscience*, 1(7),  
466 458–462, doi:10.1038/ngeo231.

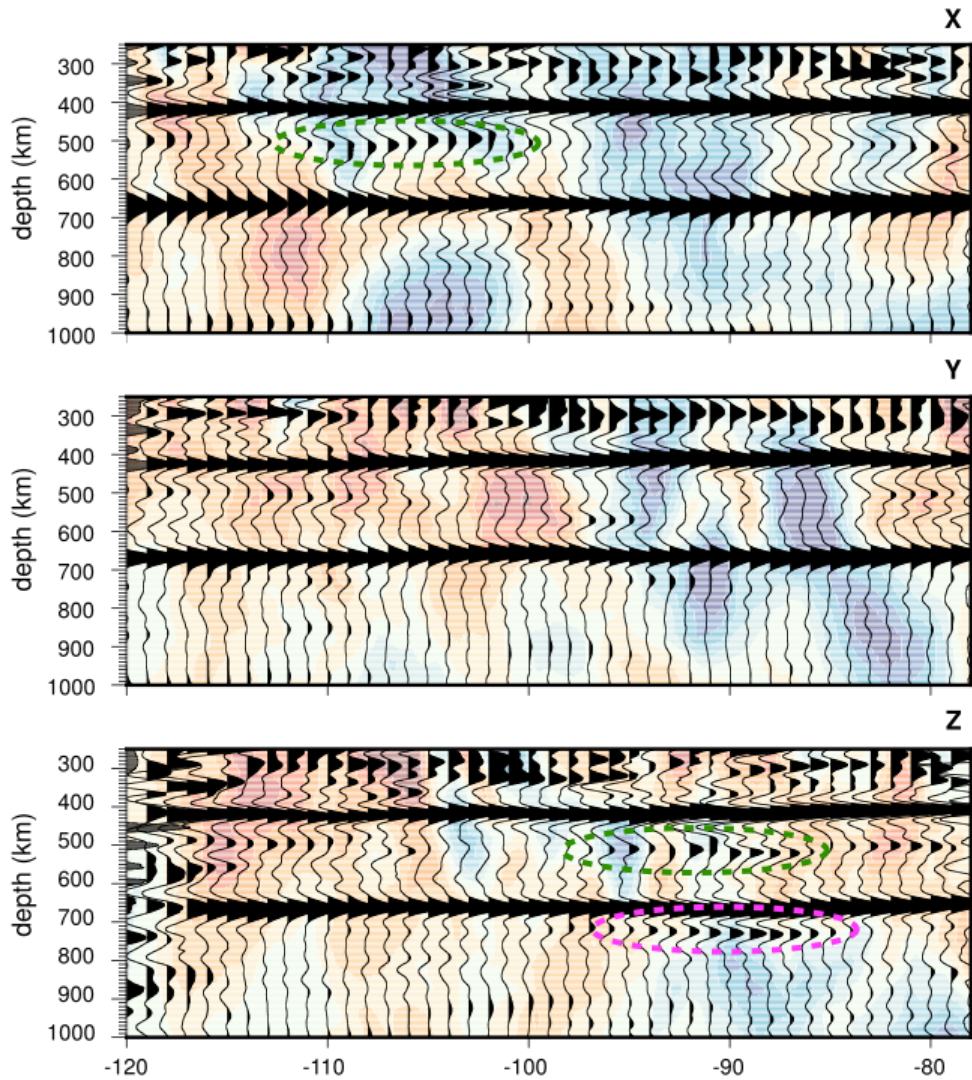
467 Simmons, N. A., and H. Gurrola (2000), Multiple seismic discontinuities near the  
468 base of the transition zone in the Earth ' s mantle, *Nature*, 405, 559–562, doi:  
469 10.1038/35014589.

470 Stixrude, L., and C. Lithgow-Bertelloni (2011), Thermodynamics of mantle minerals  
471 - II. Phase equilibria, *Geophysical Journal International*, 184(3), 1180–1213, doi:  
472 10.1111/j.1365-246X.2010.04890.x.

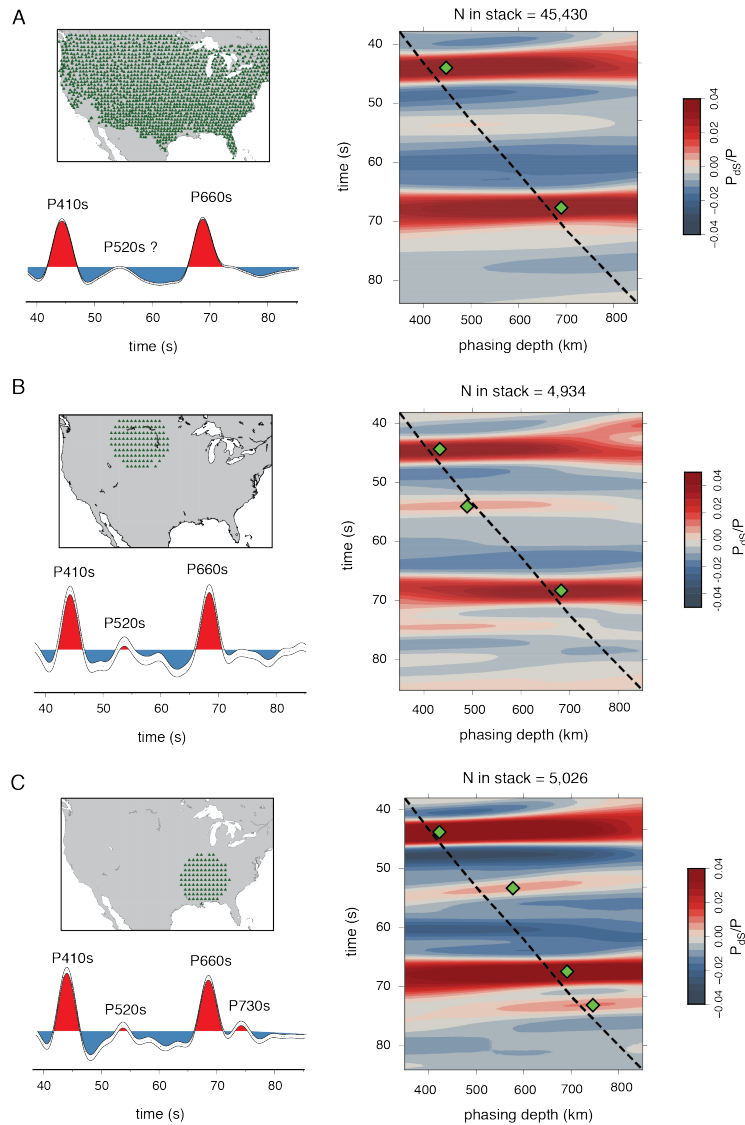
473 Tauzin, B., R. D. Van Der Hilst, G. Wittlinger, and Y. Ricard (2013), Multiple transition  
474 zone seismic discontinuities and low velocity layers below western United States, *Jour-*  
475 *nal of Geophysical Research: Solid Earth*, 118(5), 2307–2322, doi:10.1002/jgrb.50182.

476 Tauzin, B., S. Kim, and J.C. Afonso (2018), Multiple phase changes in the mantle tran-  
477 sition zone beneath northeast Asia: Constraints from teleseismic reflected and converted  
478 body-waves, *Journal of Geophysical Research: Solid Earth*, doi:10.1029/2017JB015238.

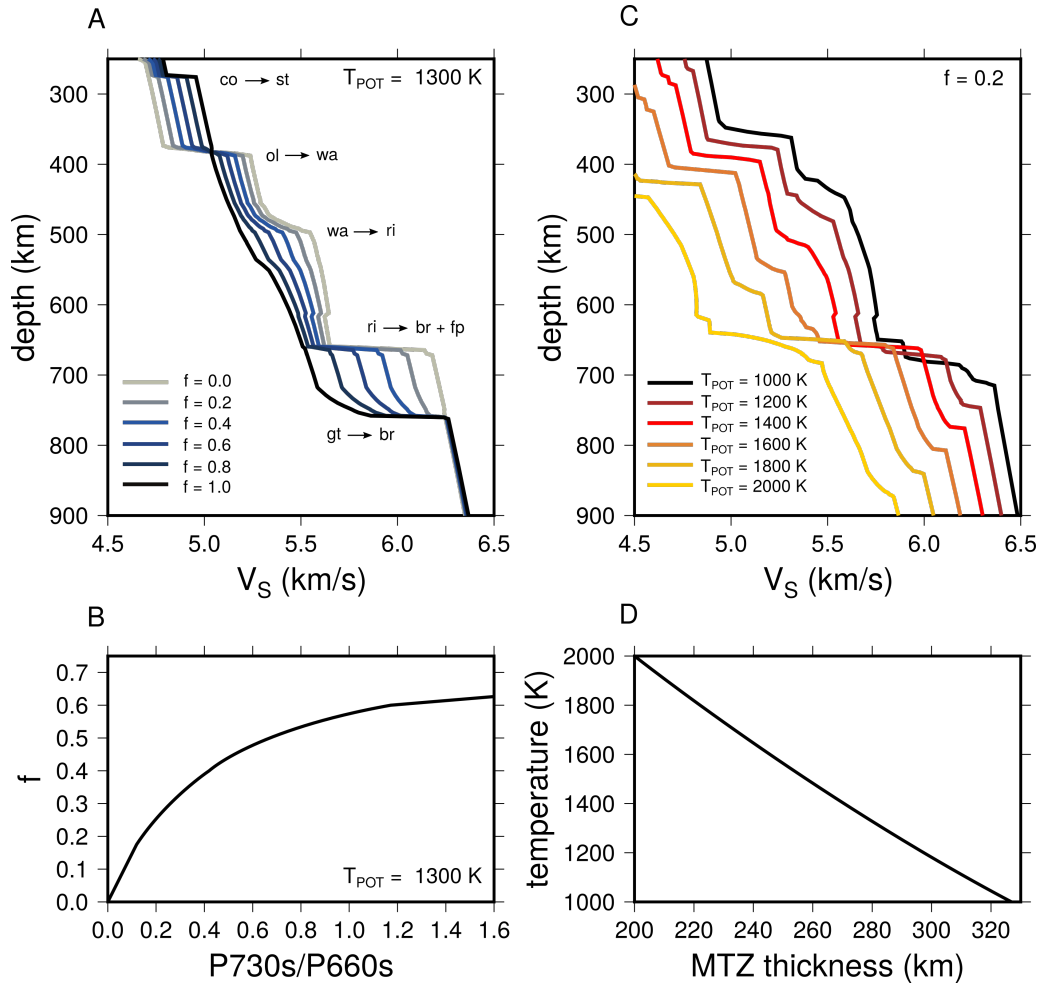
- 479 van der Lee, S., and G. Nolet (1997), Seismic image of the subducted trailing fragments  
480 of the Farallon plate, *Nature*, 386(6622), 266–269, doi:10.1038/386266a0.
- 481 Vinnik, L. (1977), Detection of waves converted from P to SV in the mantle, *Physics of*  
482 *the Earth and Planetary Interiors*, 15(1), 39–45, doi:10.1016/0031-9201(77)90008-5.
- 483 Wang, H., M. Gurnis, and J. Skogseid (2017), Rapid Cenozoic Subsidence in the Gulf of  
484 Mexico Resulting From Hess Rise Conjugate Subduction, *Geophysical Research Letters*,  
485 44(21), 10,930–10,938, doi:10.1002/2017GL074959.
- 486 Wang, X., and F. Niu (2011), Imaging the mantle transition zone beneath eastern and  
487 central China with CEArray receiver functions, *Earthquake Science*, 24(1), 65–75, doi:  
488 10.1007/s11589-011-0770-x.
- 489 Waszek, L., N. C. Schmerr, and M. D. Ballmer (2018), Global observations of reflectors  
490 in the mid-mantle with implications for mantle structure and dynamics, *Nature Commu-*  
491 *nications*, 9(1), 385, doi:10.1038/s41467-017-02709-4.
- 492 Workman, R. K., and S. R. Hart (2005), Major and trace element composition of the de-  
493pleted MORB mantle (DMM), *Earth and Planetary Science Letters*, 231(1-2), 53–72,  
494 doi:10.1016/j.epsl.2004.12.005.
- 495 Xie, S., and P. J. Tackley (2004), Evolution of helium and argon isotopes in a con-  
496necting mantle, *Physics of the Earth and Planetary Interiors*, 146(3-4), 417–439, doi:  
497 10.1016/j.pepi.2004.04.003.
- 498 Xu, W., C. Lithgow-Bertelloni, L. Stixrude, and J. Ritsema (2008), The effect of bulk  
499 composition and temperature on mantle seismic structure, *Earth and Planetary Science*  
500 *Letters*, 275(1-2), 70–79, doi:10.1016/j.epsl.2008.08.012.



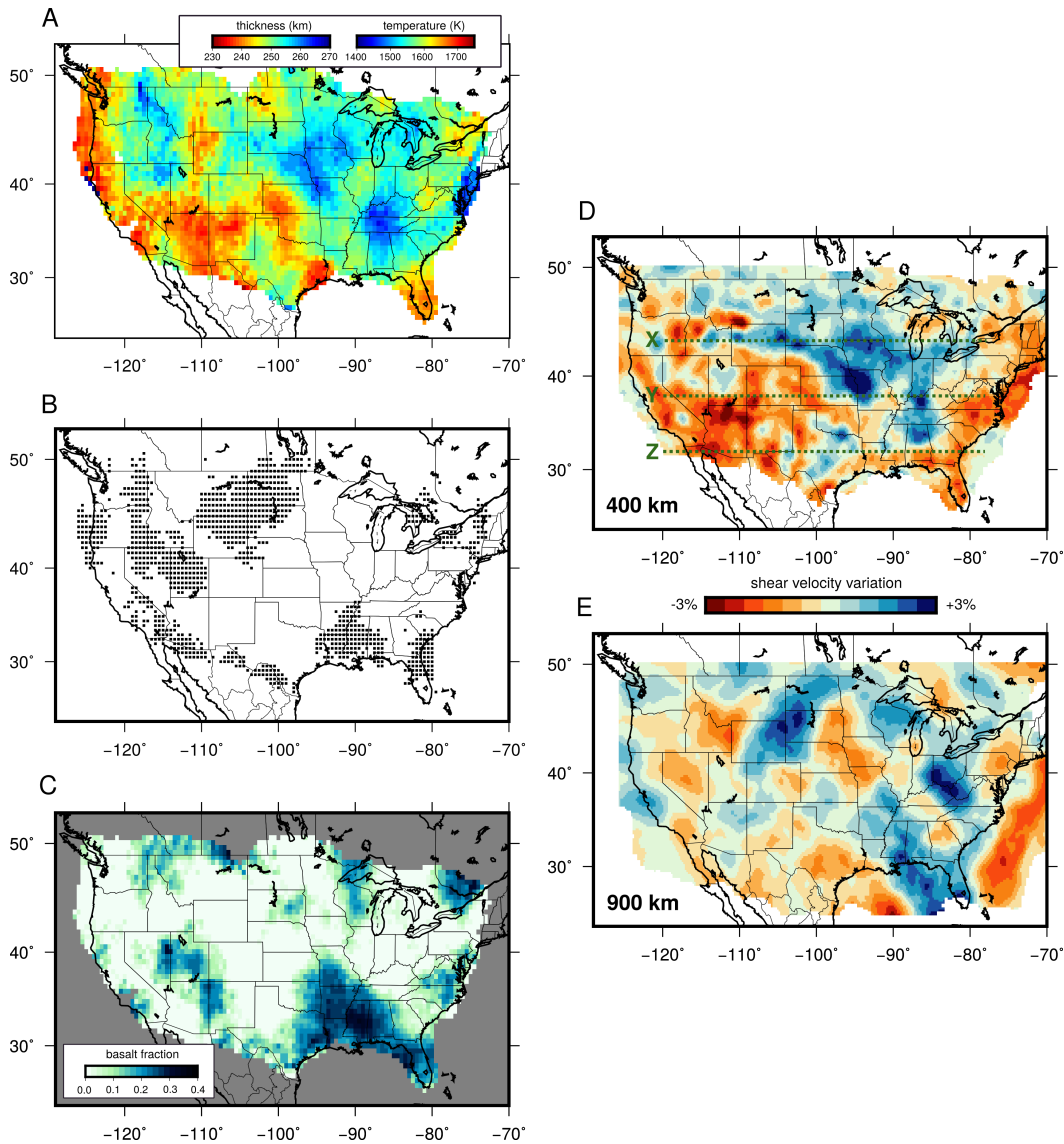
501 **Figure 1.** Longitudinal cross sections through the CCP imaging volume for (from top to bottom) latitude  
 502 44°N (profile X), 38°N (profile Y), and 32°N (profile Z). High-amplitude conversions from the 520 and 730  
 503 are indicated by green and pink circles, respectively. The background depicts the shear velocity structure of  
 504 tomographic model US-SL-2014 [Schmandt and Lin, 2014a]. The locations of the cross sections are shown in  
 505 Figure 4D.



506 **Figure 2.** Comparison between receiver function stacks of the full data set (A), and regional stacks of 4,934  
 507 receiver functions from stations in the northern Rockies (B), and 5,026 receiver functions from stations in the  
 508 southeastern US (C). Each region has three panels. The top left panel shows the included stations, the bottom  
 509 left panel shows the move-out corrected stack, and the right panel shows a phasing analysis. The move-out  
 510 corrected stacks show the average receiver function signal, as well as the upper and lower bound of the boot-  
 511 strap confidence interval. Positively identified phases are labeled. Green diamonds shown in the phasing  
 512 analysis indicate a local maximum.



513 **Figure 3.** A) Profiles of the shear velocity ( $V_S$ ) for mechanical mixtures of harzburgite and MORB as  
 514 a function of MORB fraction  $f$  along a 1300 K adiabat. B) Synthetic amplitude ratios of  $P730s/P660s$   
 515 for variable  $f$  (See Supplemental material). C)  $V_S$  profiles for varying potential temperatures with a fixed  
 516 MORB fraction of  $f = 0.2$ . D) MTZ thickness for varying temperature. Mineral phase names in A and C are  
 517 as follows: coesite ( $co$ ), stishovite ( $st$ ), olivine ( $ol$ ), wadsleyite ( $wa$ ), ringwoodite ( $ri$ ), brigmanite ( $br$ ), fer-  
 518 ropericlasite ( $fp$ ), majorite garnet ( $gt$ ). The 300, 410, 520, 660, and 730 correspond to the  $co \rightarrow st$ ,  $ol \rightarrow wa$ ,  
 519  $wa \rightarrow ri$ ,  $ri \rightarrow br + fp$ , and  $gt \rightarrow br$  mineral transitions, respectively.



520 **Figure 4.** The maps on the left show (A) the thickness of the transition zone from  $P_{660s}$ – $P_{410s}$  arrival  
 521 times and the potential temperature as inferred from predicted seismic velocity profiles of MM pyrolite, (B)  
 522 regions where  $P_{520s}$  is detected with an amplitude of at least 20% of  $P_{410s}$ , and (C) the inferred basalt  
 523 fraction based on the  $P_{730s}/P_{660s}$  amplitude ratio. The maps on the right show shear velocity variations at  
 524 depths of 400 km (D) and 900 km (E) according to model US-SL-2014. The dashed lines in D indicate the  
 525 transects X, Y, and Z of the CCP cross sections shown in Figure 1.

Figure 1.

Author Manuscript

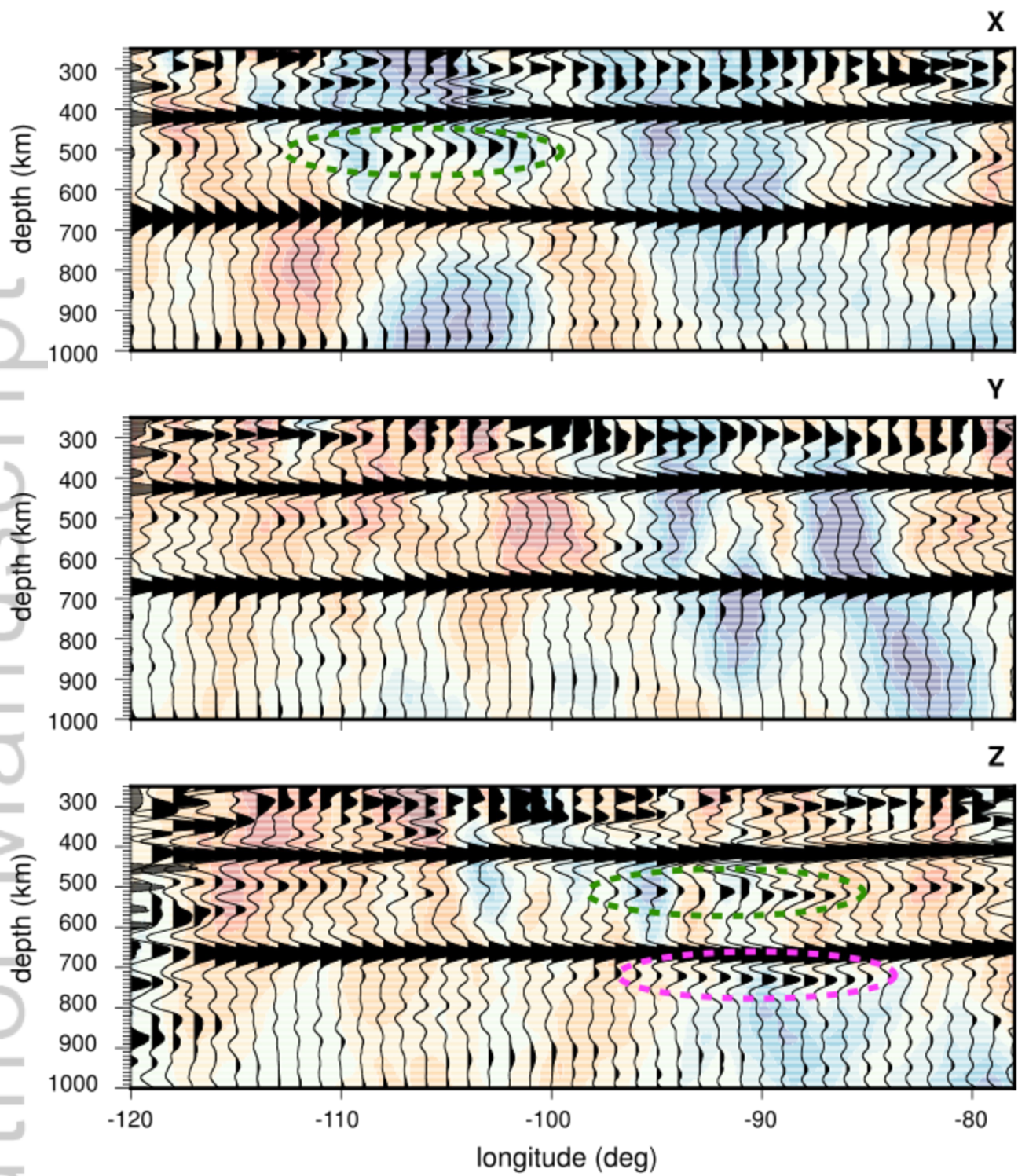


Figure 2.

Author Manuscript

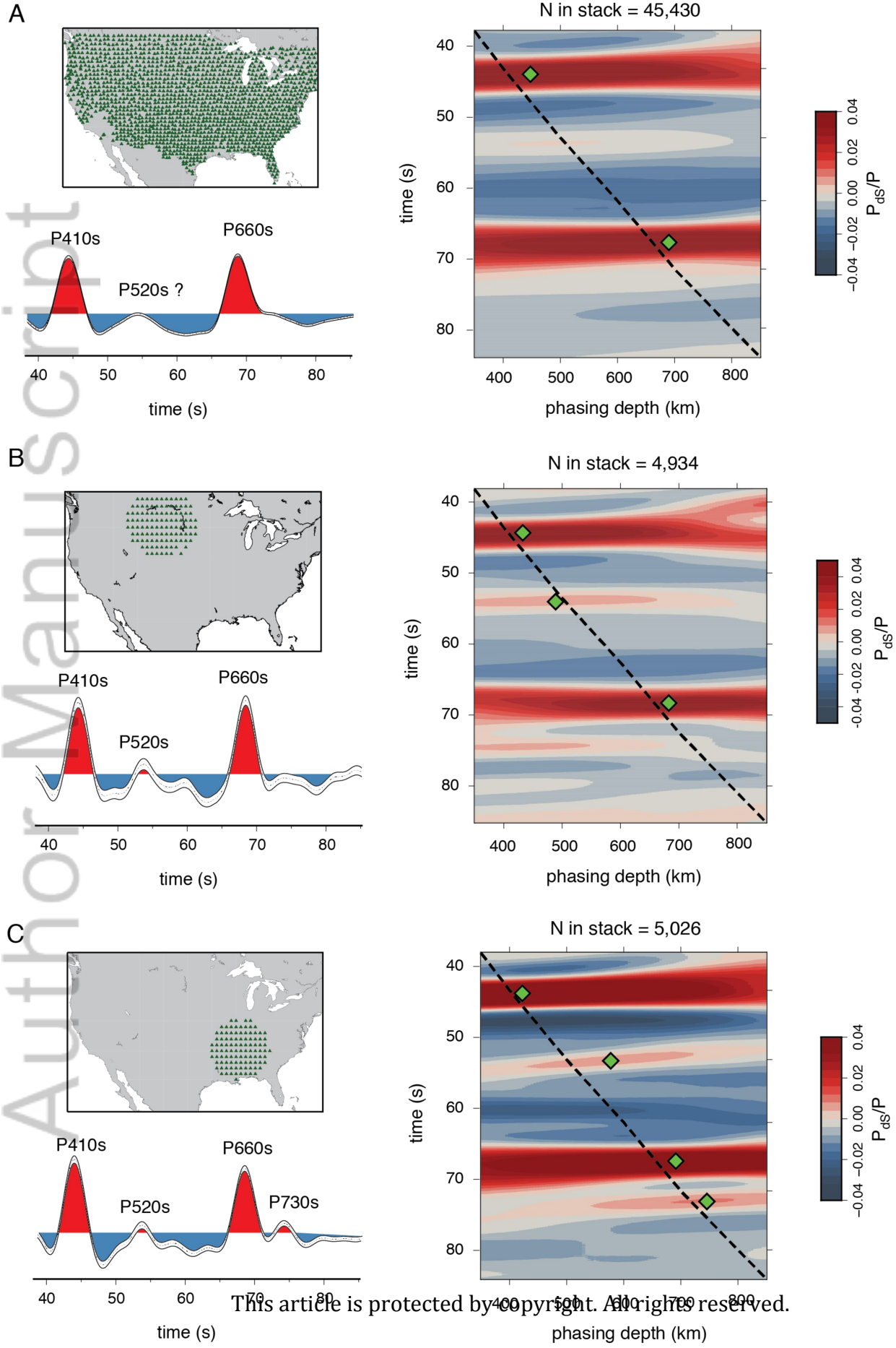


Figure 3.

Author Manuscript

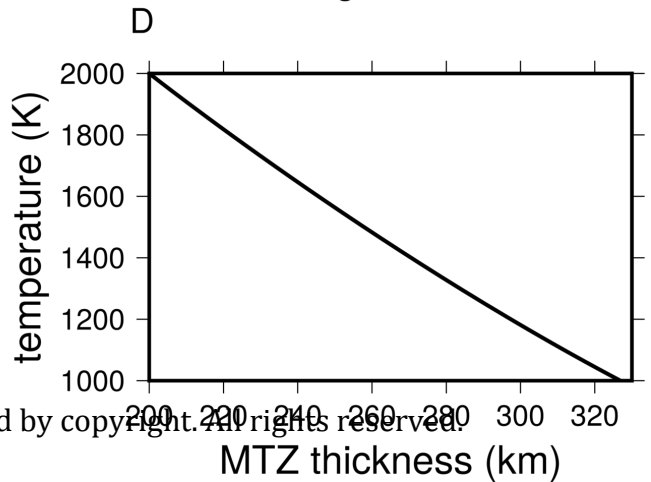
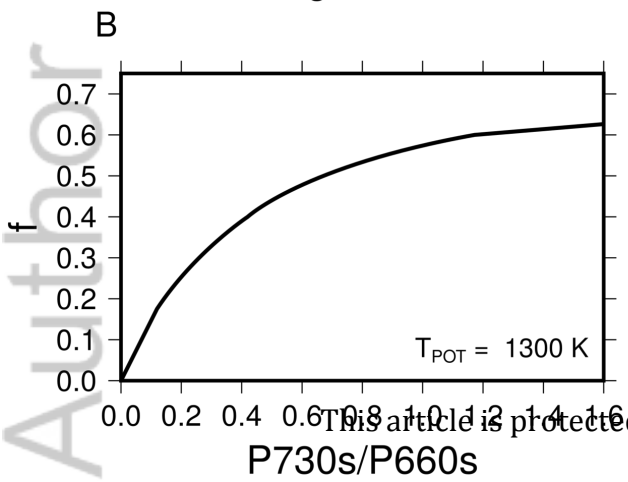
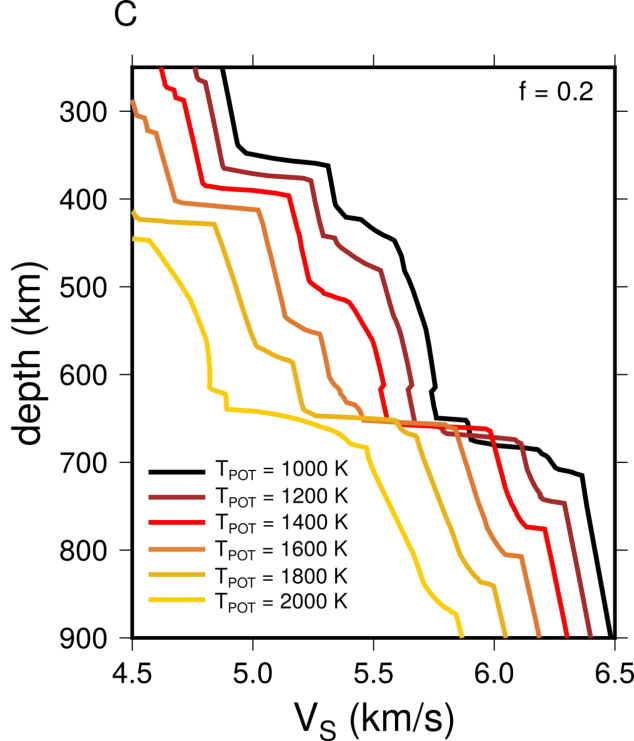
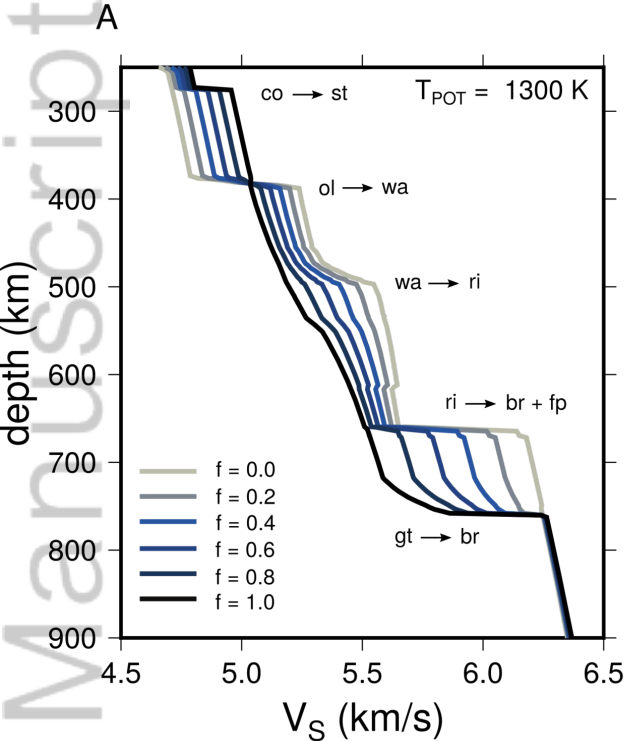
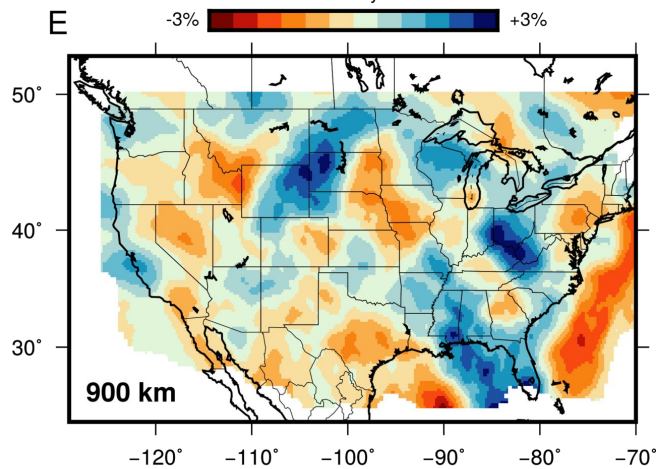
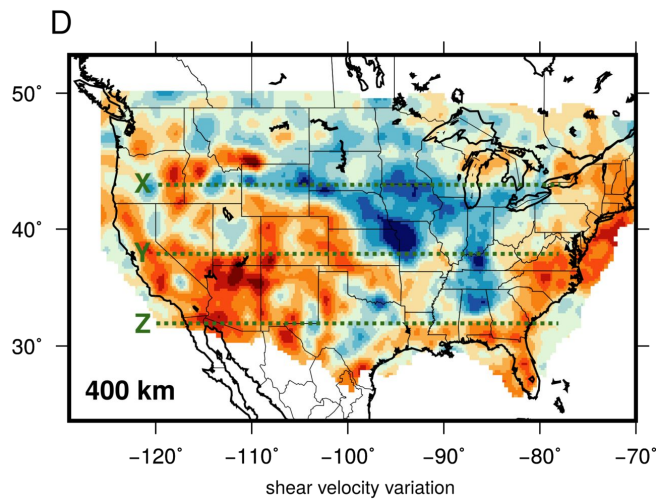
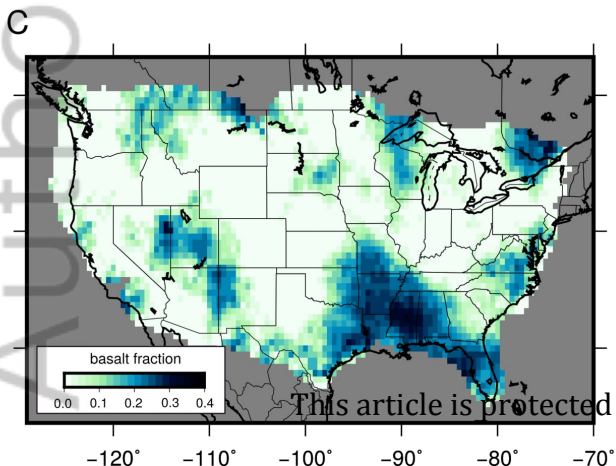
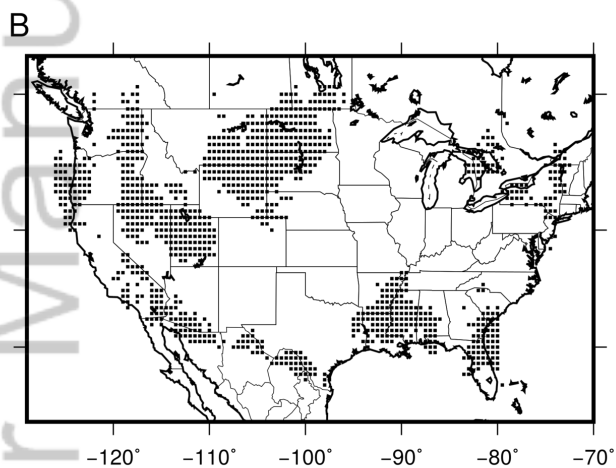
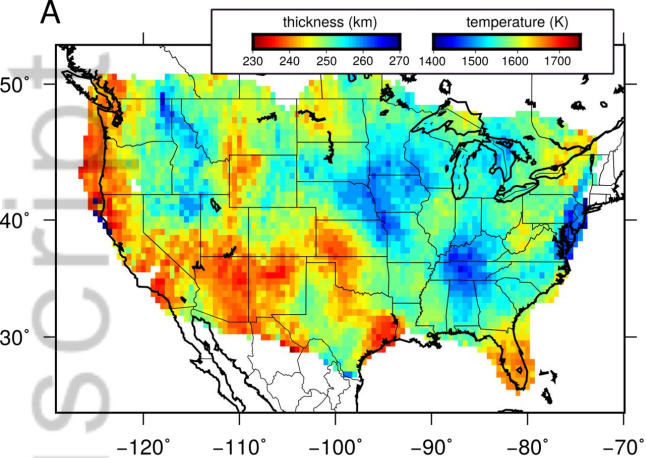
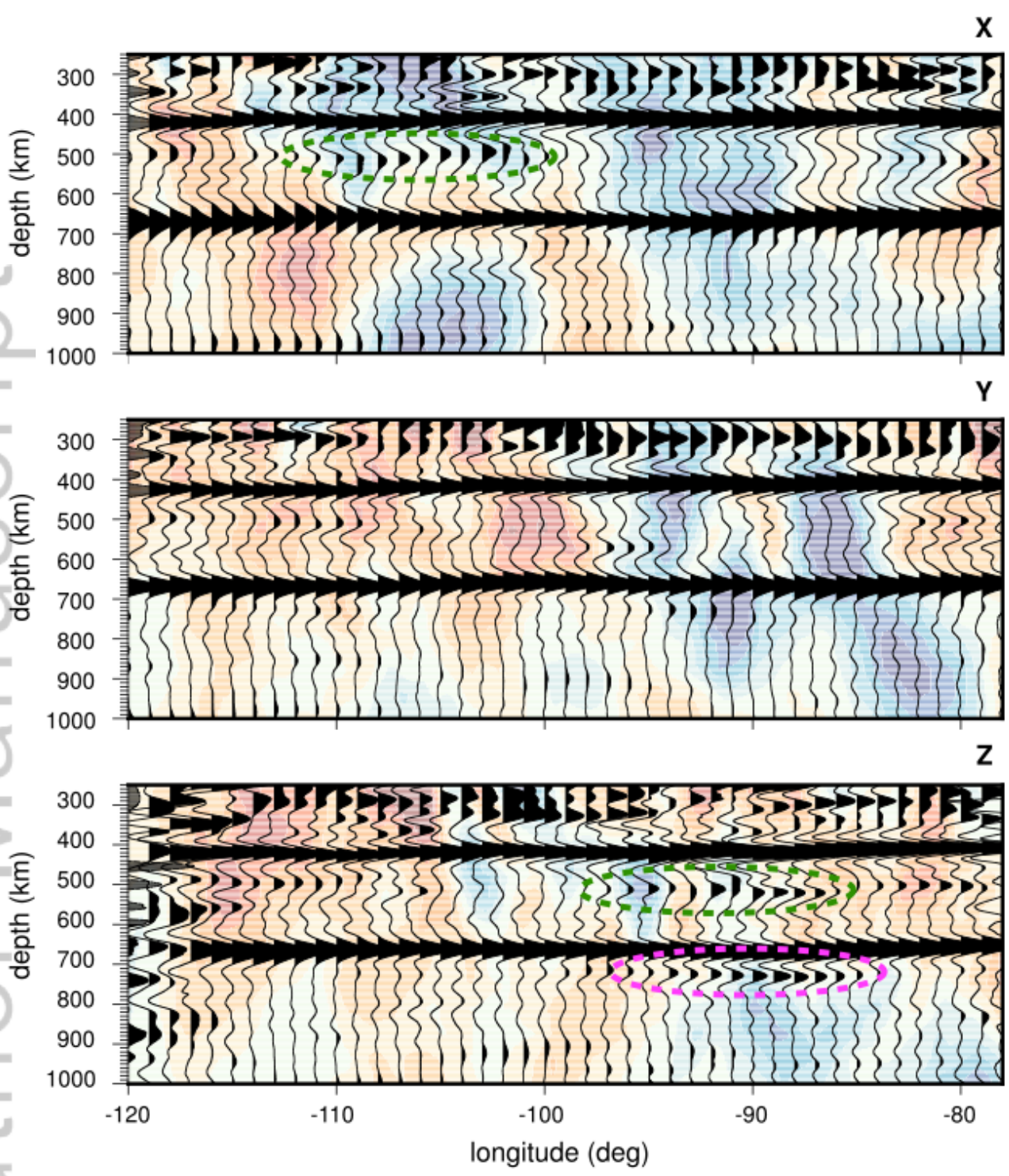


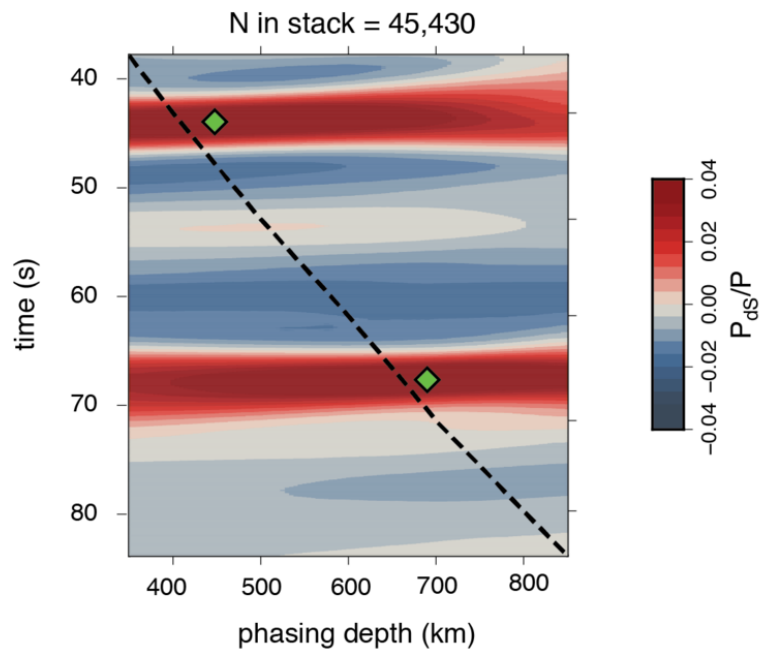
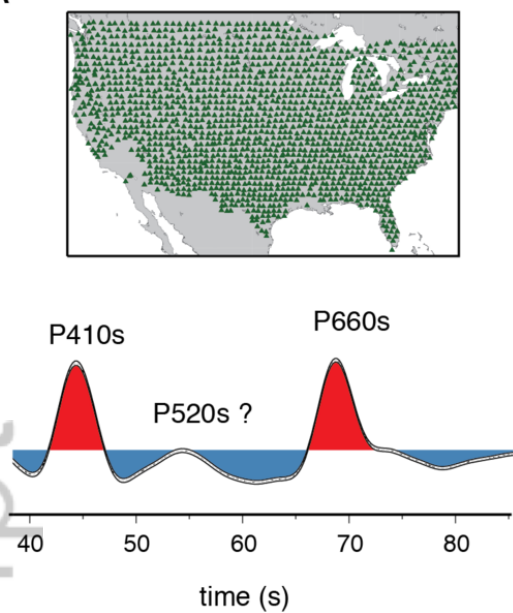
Figure 4.

Author Manuscript

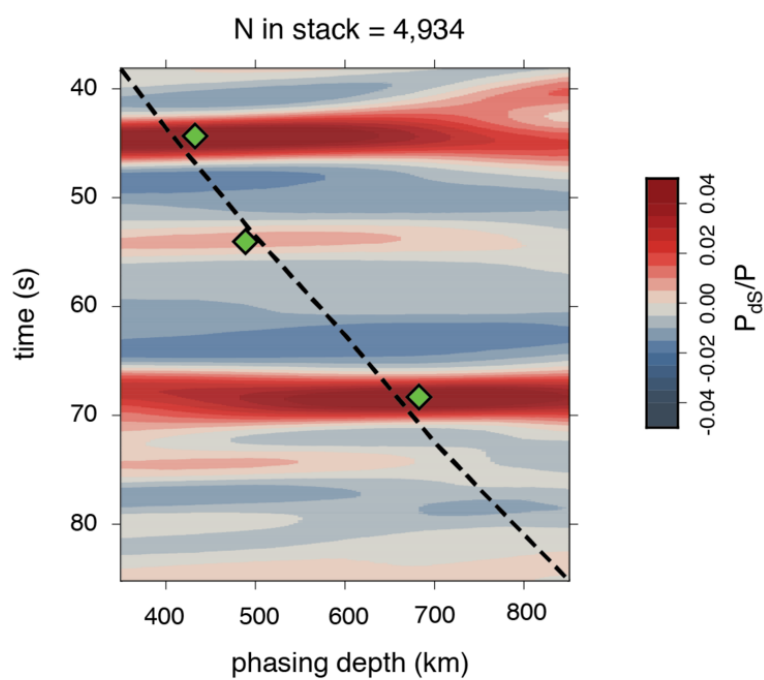
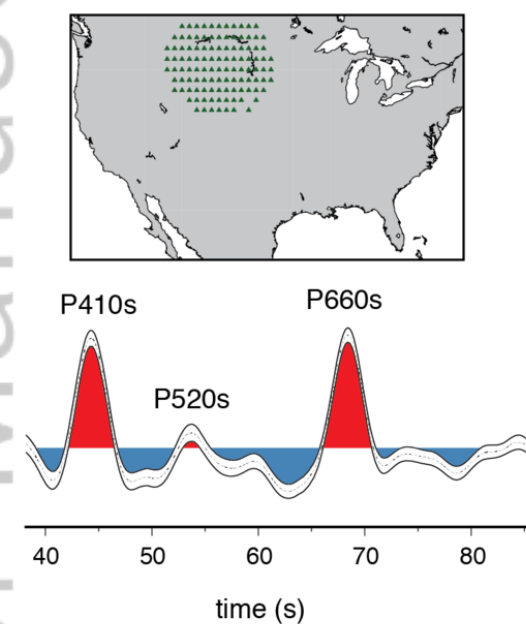




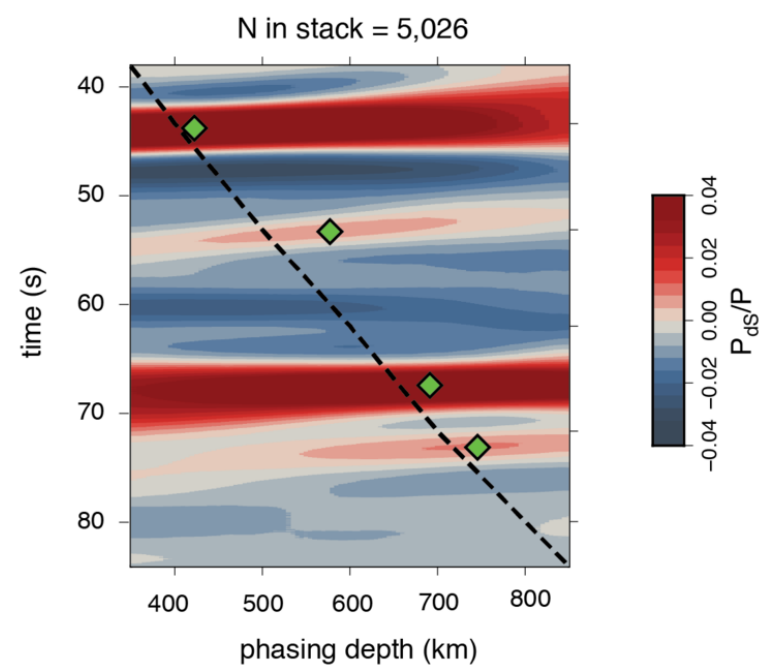
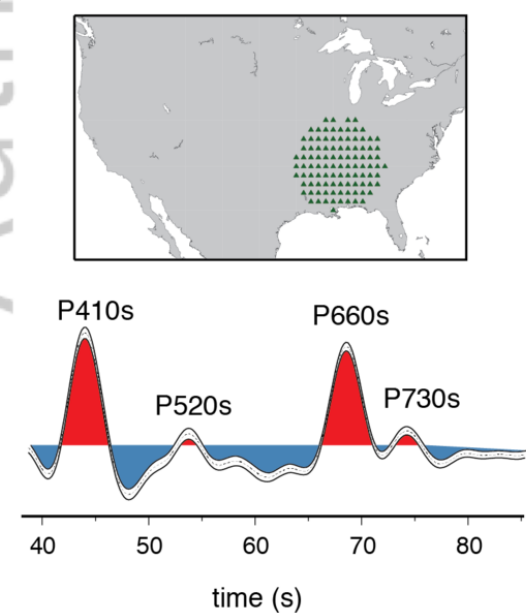
A



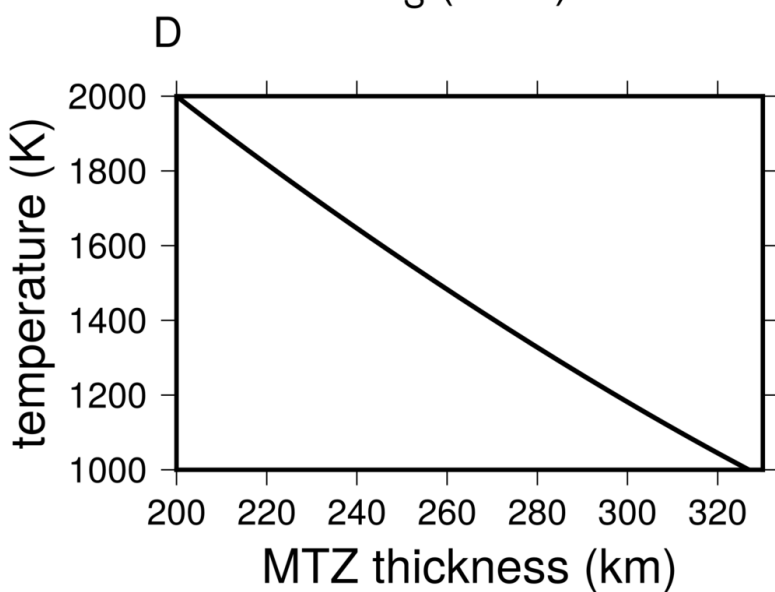
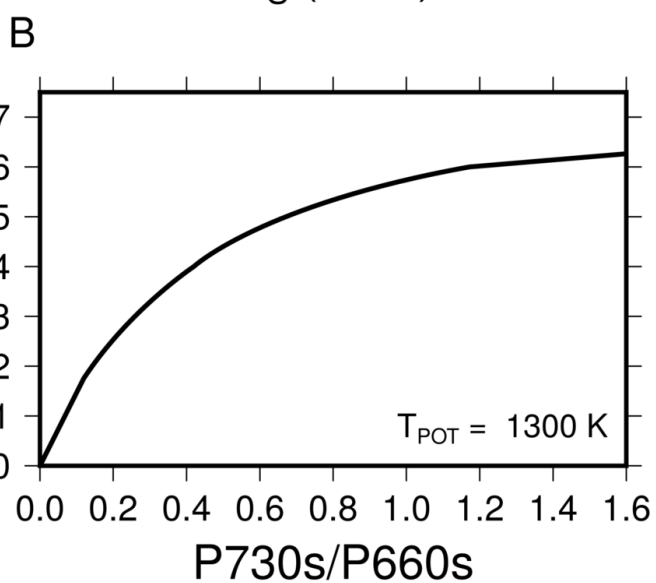
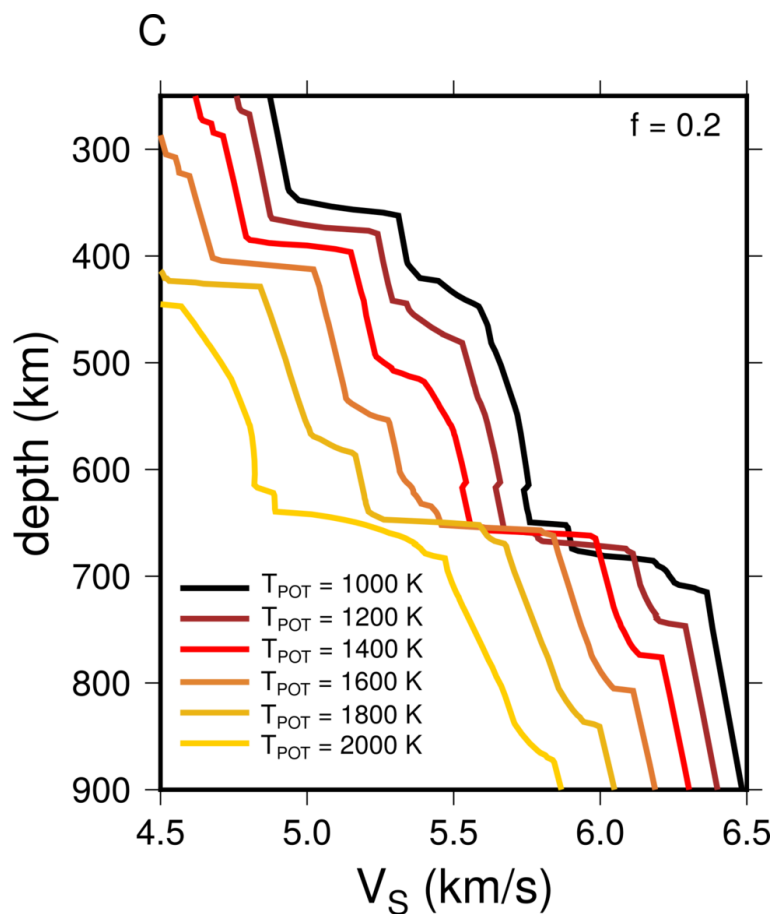
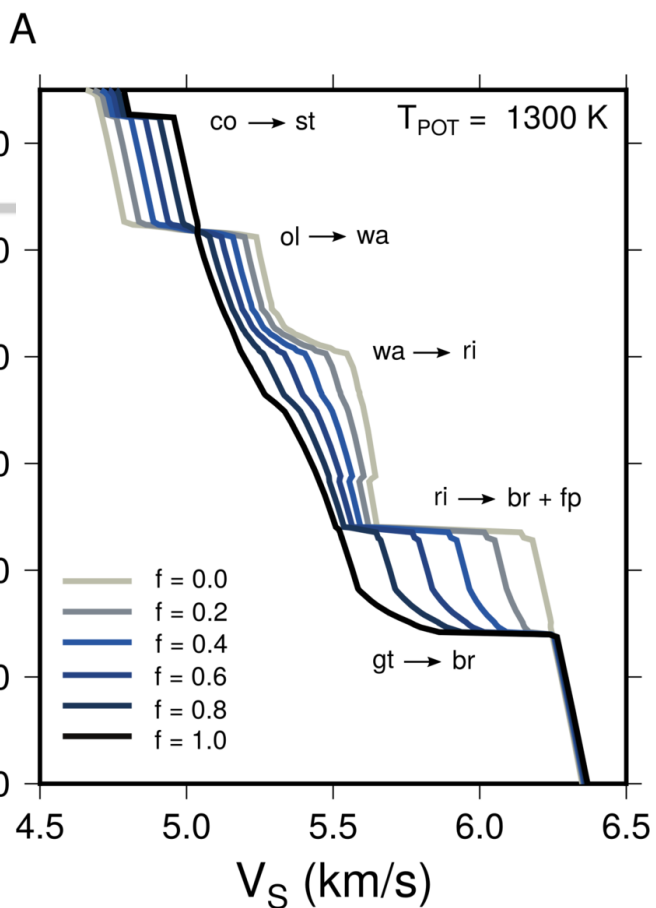
B



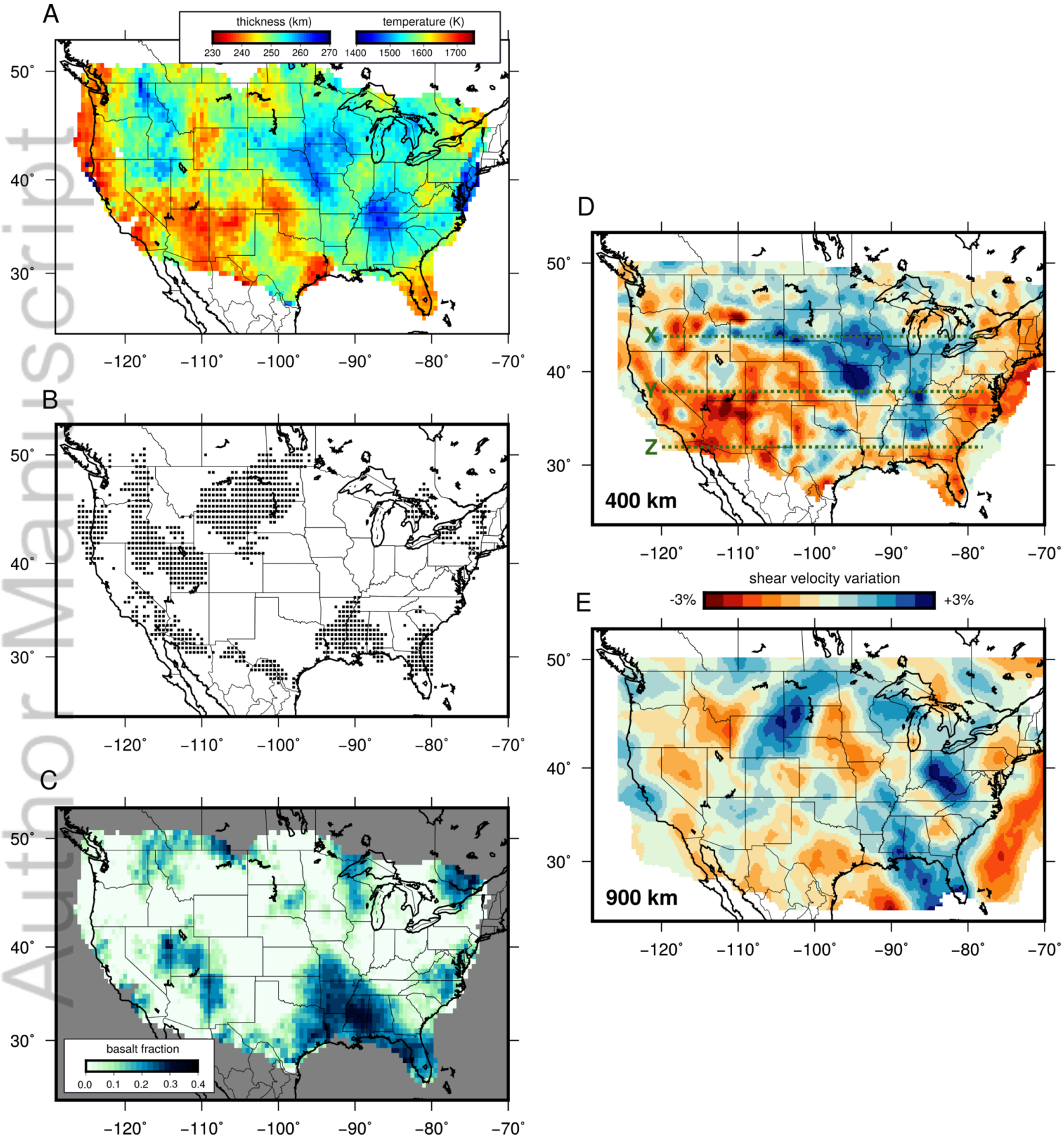
C



2018GL078378-f02-z.png



2018GL078378-f03-z-.png



2018GL078378-f04-z-.png